

LENSING PROBABILITIES FOR SPECTROSCOPICALLY SELECTED GALAXY-GALAXY STRONG LENSES

GREGORY DOBLER^{1,5}, CHARLES R. KEETON², ADAM S. BOLTON^{1,3}, AND SCOTT BURLES⁴

Draft version October 25, 2018

ABSTRACT

Spectroscopic galaxy-galaxy lens searches are presently the most prolific method of identifying strong lens systems in large data sets. We study the probabilities associated with these lens searches, namely the probability of identifying a candidate with rogue [O II] emission lines in a galaxy’s spectrum, and the probability that the candidate will show features of strong lensing in follow-up photometric observations. We include selection effects unique to spectroscopic data, and apply them to the Sloan Lens ACS (SLACS) survey (Bolton et al. 2006). The most significant selection effect is the finite size of the spectroscopic fiber which selects against large separation lenses and results in a non-monotonic dependence of the rogue line probability on velocity dispersion. For example, with the 3 arcsec diameter SDSS fiber and 2 arcsec FWHM seeing, we find that the probability that a given LRG has a rogue [O II] line in its spectrum *decreases* with velocity dispersion from 150 km/s to 300 km/s and then increases up to 400 km/s for a given source size. The total probability for observing a rogue line in a single survey spectrum is $\sim 0.9\text{--}3.0\%$, and the total lensing rate is $\sim 0.5\text{--}1.3\%$. The range is due to uncertainties in the physical size of [O II] emission regions, and in the evolution of the [O II] luminosity function. Our estimates are a factor of ~ 5 higher than the results of the SLACS survey, a discrepancy which we attribute to the SLACS requirement that multiple rogue lines be observed simultaneously.

Subject headings: gravitational lensing – surveys – galaxies: statistics

1. INTRODUCTION

Spectroscopic gravitational lens searches have begun to yield a remarkable number of strong galaxy-galaxy (g-g) lens systems (Bolton et al. 2004, 2006; Willis et al. 2006). These finite source lenses promise both new physical insights and new phenomenology. The extended images provide extensive constraints on the lens potential, especially on the radial density profile, which is still the main systematic uncertainty in lensing constraints on the Hubble constant (e.g., Keeton & Kochanek 1997; Kochanek 2002). In present surveys, limits on the source redshift range mean the lenses that are found typically have images that appear well within the effective radius of the lens galaxy (Koopmans et al. 2006). This makes g-g lenses ideal for probing the inner regions of distant elliptical galaxies. In addition, current selection effects favor star-forming source galaxies, which opens the exciting possibility of observing multiply-imaged supernovae (Oguri & Kawano 2003; Dobler & Keeton 2006).

The basic premise behind spectroscopic lens searches is to mine large samples of galaxy spectra looking for “rogue” emission lines that originate from background galaxies at small impact parameter (Warren et al. 1996; Willis 2000). This technique is complementary to photometric searches (e.g., Cabanac et al. 2007; Kubo & Dell’Antonio 2007) which look for strongly lensed, arc-like features in imaging data.

Among several recent spectroscopic searches (Bolton et al. 2004, 2006; Willis et al. 2006), the most prolific has been the Sloan Lens ACS (SLACS) survey.⁶ For this survey, Bolton et al. (2004) and Bolton et al. (2006) mined a catalog of 50,996 Sloan Digital Sky Survey (SDSS) Luminous Red Galaxy (LRG, see Eisenstein et al. 2001) spectra for rogue [O II] 3727 emission lines, and found ~ 50 candidates. The addition of later SDSS data releases as well as spectra from the MAIN galaxy sample increased the number of candidates to ~ 200 , with a similar 1-in-1000 incidence. Follow-up observations have subsequently confirmed 70–80 new g-g lenses from among these candidates. SLACS data have been used to place the lens galaxies on the fundamental plane (Treu et al. 2006; Bolton et al. 2007), to constrain the redshift evolution of the density profiles of elliptical galaxies (Koopmans et al. 2006), and to trace the density profiles out to very large radii (Gavazzi et al. 2007).

Given that galaxy-galaxy lenses are already numerous, and will become increasingly common in large surveys (Marshall et al. 2005; Moustakas et al. 2007), a sound statistical analysis of the expected incidence of g-g strong lensing is warranted. In traditional analyses of the statistics of lensed quasars (e.g., Turner et al. 1984) the primary statistical question is, “what is the probability that a given source is lensed?” By contrast, in g-g lens statistics the question is different, viz. “what is the probability that a given galaxy is a lens?” In this paper we formulate a general statistical analysis applicable to spectroscopic g-g lens searches, and apply it to the SLACS sample to estimate the total number of rogue emission lines in the survey, and the actual number of strong lens systems that should be confirmed by follow-up observations. Our re-

¹ Harvard-Smithsonian Center for Astrophysics, 60 Garden Street, Cambridge, MA 02138 USA

² Department of Physics and Astronomy, Rutgers University, 136 Frelinghuysen Road, Piscataway, NJ 08854 USA

³ B.W. Parrent Fellow, Institute for Astronomy, University of Hawaii, 2680 Wodlawn Dr., Honolulu, HI 96822, USA

⁴ Kavli Institute for Astrophysics and Space Research and Department of Physics, Massachusetts Institute of Technology, Cambridge, MA 02139 USA

⁵ gdobler@cfa.harvard.edu

⁶ www.slacs.org

sults for SLACS will help assess the completeness of that survey, while our general conclusions will (we hope) be useful in the design of future spectroscopic lens searches.

Except where noted, throughout this paper we assume a flat cosmology with $\Omega_M = 0.3$, $\Omega_\Lambda = 0.7$, and $H_0 = 70$ km/s/Mpc.

2. PROBABILITY FOR GALAXY-GALAXY LENSING

Figure 1 shows a schematic representation of the lensing geometry. Let the galaxy be described by a singular isothermal ellipsoidal (SIE) mass distribution with parameters $\vec{G} = (z_l, \sigma, e, \gamma, \phi_\gamma)$ where z_l is the redshift, σ is the velocity dispersion, e is the ellipticity, γ is the external shear, and ϕ_γ is the angle between the ellipticity and shear. The probability $P_G(\vec{G})$ that this galaxy is a lens is equivalent to the probability that there is a source within the ‘‘Einstein cone’’ of the galaxy. Here we define the Einstein cone to be the region behind the galaxy in which a source is strongly lensed. For point sources, the Einstein cone is the same as the multiply-imaged region, but we will refine the definition shortly to incorporate complexities from extended sources. Note that the cross section of this region need not be circular, and its size does not grow linearly with distance, so the volume is not strictly conical; but we believe the terminology is convenient and attractive.

If the number density of sources brighter than flux S as a function of redshift is given by $n_s(z_s, S)$, then the lensing probability is

$$P_G(\vec{G}) = \int_{V_{\text{ein}}} n_s(z_s, S) dV \quad (1)$$

$$= \int_{z_l}^{\infty} \frac{dV}{dz_s d\Omega} dz_s \int n_s(z_s, S) d\vec{u},$$

where V_{ein} is the volume of the Einstein cone, z_l and z_s are the lens and source redshifts respectively, and $\Omega = \Omega(z_s)$ is the solid angle subtended by the cone at z_s . The integral over Ω is actually an integral over \vec{u} , the angular coordinates in the source plane, and for now we consider the source plane integral to extend over the multiply-imaged region. Finally, it is natural to do the integral in comoving coordinates, but to express distances as angular diameter distances. So we write the comoving volume element as

$$\frac{dV}{dz_s d\Omega} = \frac{c}{H_0} \frac{(1+z_s)^2 D_s^2}{E(z_s)}, \quad (2)$$

where $E(z) = [\Omega_M(1+z)^3 + \Omega_\Lambda]^{1/2}$, and write factors of $(1+z_s)$ explicitly allow us to keep D_s as the angular diameter distance to the source.

In practice, we are interested in the number density of sources whose observed flux is above a survey’s flux limit S_0 . This implies $S_I \times \mu \geq S_0$ where S_I is the source’s intrinsic flux and μ is the lensing magnification. Therefore, the relevant number density for eq. (1) is

$$n_s(z_s, S) = n_s(z_s, S_0/\mu) = \int_{L_0/\mu}^{\infty} \Phi(L, z_s) dL, \quad (3)$$

where $\Phi(L, z_s)$ is the source luminosity function at redshift z_s . Here $L_0 = 4\pi(1+z_s)^4 D_s^2 S_0$ is the luminosity corresponding to the flux limit S_0 , and factors of $(1+z_s)$

again appear so that we may keep D_s as an angular diameter distance. The fact that the lower limit of integration depends on μ means that the integral automatically incorporates lensing magnification bias.

With point sources the definition of a lens relies on image multiplicity: any source with multiple images is said to be strongly lensed. With extended sources the situation is more complicated. A source lying just outside the caustics might be distorted enough to be labeled a lens even if there is just one image. A source lying astride a cusp or fold caustic may exhibit a single arc comprising two or three merged images, with counter-images that may or may not be bright enough to be detectable. The point is that identifying an object as a lens may depend on some qualitative interpretation of the morphology. Since the interpretation depends on distortions of the image(s), which are related to the lensing magnification, we attempt to quantify the labeling of extended lenses through a magnification cut. Specifically, we label an object a lens if the lensing magnification μ exceeds some threshold set by μ_{cut} . (Our choice of μ_{cut} is discussed below.) We then take the source plane integral in eq. (1) to extend over the region in which $\mu > \mu_{\text{cut}}$.

The lensing magnification depends not only on the source position \vec{u} , but also on the parameters of the lens galaxy. Therefore eq. (1) represents the lensing probability for a particular galaxy. To describe a population of galaxies, in principle we want to average over some appropriate distributions of z_l , σ , e , γ , and ϕ_γ . In practice, if we have a set of N observed galaxies, each of which is described by the parameters \vec{G}_i , we can do the average explicitly:

$$\bar{P}_G = \frac{1}{N} \sum_{i=1}^N P_G(\vec{G}_i). \quad (4)$$

In the following sections we apply this P_G calculation to the SLACS sample, specifically incorporating parameters and selection effects appropriate to that survey.

3. SLACS SURVEY PARAMETERS

3.1. Spectroscopic Selection Effects

When discussing SDSS spectra, it is crucial to account for the finite size of the spectroscopic fiber. The strength of a rogue emission line is directly related to how much flux from the source galaxy falls within the fiber. If a lens galaxy is massive, the lensed images may be pushed outside of the fiber, so the rogue line may be weak or even absent despite the fact that the system is a lens. Figure 2 shows a sample image configuration both with and without this ‘‘fiber cut’’ taken into account. (This figure ignores the effects of seeing, which are discussed in §4.2.)

The diameter of the SDSS fiber is 3.0 arcsec, while an SIE galaxy lens with redshift $z_l = 0.2$ and velocity dispersion $\sigma = 250$ km/s (roughly the mean LRG redshift and velocity dispersion from the SLACS survey) has an Einstein radius of ~ 1.0 – 1.2 arcsec depending on z_s . Thus, the fiber cut may create a significant bias against large separation lenses in the SLACS sample. There is also a bias against large sources (for a given source flux). Of course, with follow up observations the full image configuration will be observed, but it is the fiber flux that

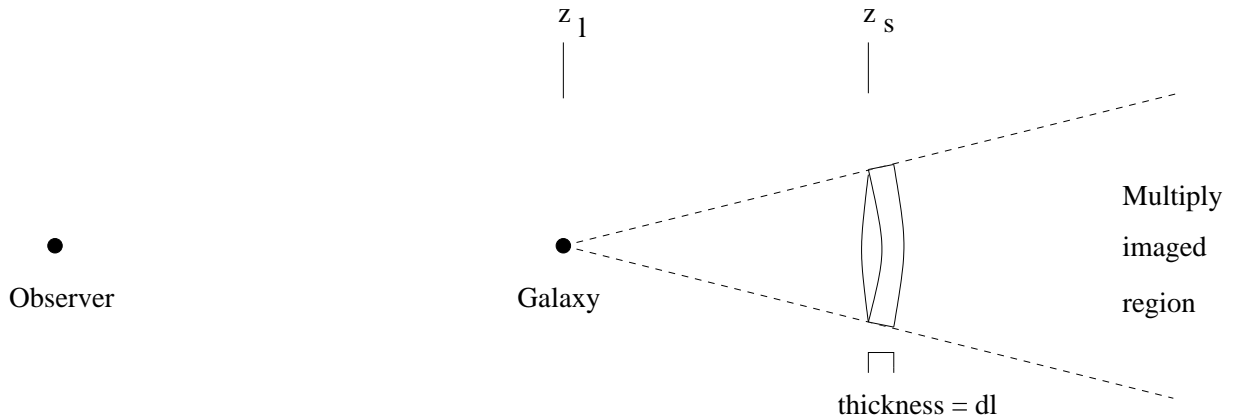


FIG. 1.— Lensing geometry for spectroscopically-selected galaxy-galaxy lenses. The probability that the foreground galaxy is a lens is the probability that there is a source within the galaxy’s “Einstein cone.” (The multiply-image region behind the galaxy is not strictly a cone, because the cross section need not be circular and does not grow linearly with distance; but the terminology is attractive.)

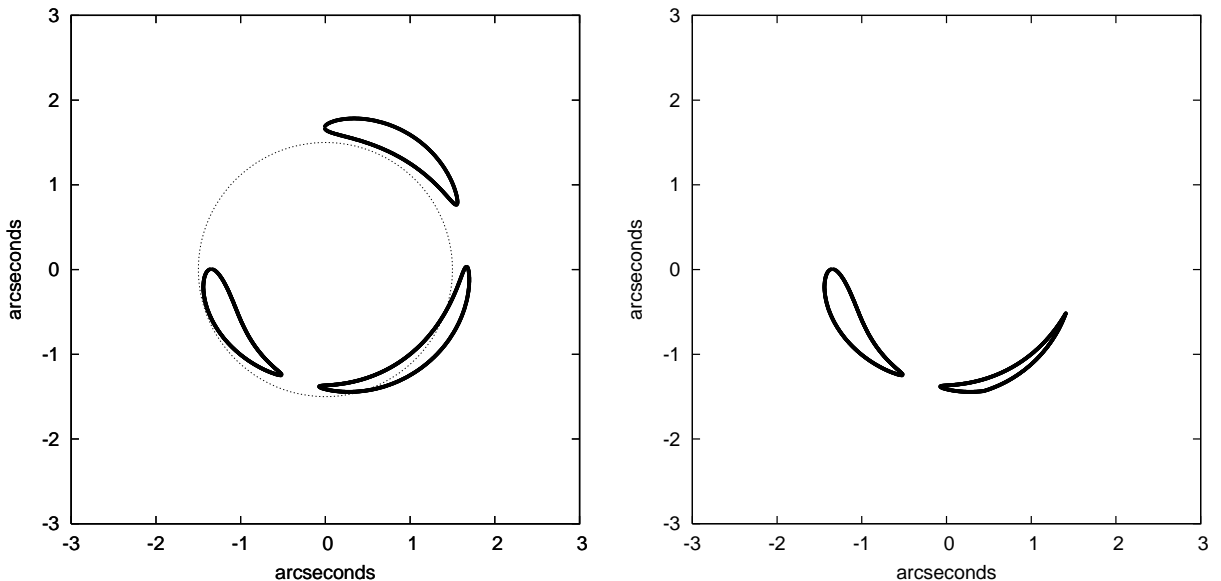


FIG. 2.— Selection effects due to the finite SDSS spectroscopic fiber size. (*Left*) The solid curves show a sample image configuration for a lens system with lens parameters $(z_l, \sigma, e, \gamma, \phi_\gamma) = (0.2, 300 \text{ km/s}, 0.3, 0.05, 0.0)$ and source parameters $(z_s, R_{\text{src}}, u_0, v_0) = (0.6, 0.88 \text{ kpc}, 0.15'', 0.15'')$. The dotted circle denotes the SDSS fiber. (*Right*) The solid curves show only the portion of the images that fall inside the fiber. The fiber cut reduces the integrated flux within the fiber, creating a selection bias against large separation lenses and large source sizes. (This figure ignores the effects of seeing, which are discussed in §4.2.)

determines whether a system is identified as a lens candidate in the first place.

The finite wavelength range of SDSS spectra places an upper limit on detectable source redshifts. The quality of spectral noise modeling is another important factor, since imperfect sky subtraction can leave emission line residuals that are not modeled by the eigenspectra used to fit LRGs (see Figure 1 of Bolton et al. 2004). Bolton et al. (2004) were careful to account for imperfect sky subtraction at long wavelengths, allowing them to probe deep into the 7000–9000 Å range. A third factor is the SLACS selection criteria: LRG spectra were required to exhibit not only blended [O II] 3727 lines, but also two longer-wavelength “secondary” features. The longest-wavelength secondary feature was

[O III] 5007, while the shortest was $H\beta$ with rest wavelength 4863 Å. These lead to an upper limit on the source redshift of $z_{s,\text{max}} \sim 9200\text{Å}/5007\text{Å} - 1 = 0.84$ and $z_{s,\text{max}} \sim 9200\text{Å}/4863\text{Å} - 1 = 0.89$, respectively. In our calculations we therefore take $z_{s,\text{max}} = 0.9$. Finally, to ensure a significant lensing probability in their sample, Bolton et al. (2004) only searched for sources with velocities more than 5000 km/s behind the LRG, corresponding to a lower limit on the source redshift of $z_{s,\text{min}} = z_l + 0.017$. These constitute the limits of the z_s integration in eq. (1).

The last important spectral parameter is the flux limit. Figure 1 of Bolton et al. (2004) shows the typical 1σ noise spectrum. For wavelengths $\lesssim 7200$ Å the wavelength dependence is small, so for simplicity we take

TABLE 1
SOURCE O II LF PARAMETERS

n_* (10^{-3} Mpc $^{-3}$)	$\log L_*$ (erg/s)	α	β
4.09	42.34	-1.15	0
2.16	42.31	-1.13	1
0.90	42.37	-1.17	2
0.62	42.18	-1.09	3

NOTE. — Best-fit Schechter function parameters for the O II luminosity function in the redshift range $0.3 < z < 1.5$. We have converted the data of Hogg et al. (1998) from Λ CDM to Λ CDM, and we have considered different possibilities for the number evolution parameter β (see text).

the noise floor to be constant in wavelength, which also means constant in source redshift. Including the Bolton et al. (2004) requirement that secondary emission features have signal-to-noise ratios greater than 3.0, we take $S_0 = 6.0 \times 10^{-17}$ ergs/s/cm 2 .

3.2. Source Population: O II Luminosity Function

From eq. (3) it is clear that we must specify the luminosity function (LF) of sources, in order to account for the flux limit and the magnification bias. For SLACS, the primary selection is on [O II] line flux. Hogg et al. (1998) give the [O II] LF for the redshift range $0.3 < z < 1.5$ (see their Fig. 7), which covers the range of source redshifts accessible in the SLACS survey. However, we make two refinements to the LF. First, Hogg et al. quoted the LF for an Λ CDM cosmology, but we prefer to work in Λ CDM; luminosities and volumes both need to be adjusted. Second, since [O II] emission is thought to trace the star formation rate, the LF may vary substantially with redshift (Kennicutt 1992; Glazebrook et al. 2003). We include the possibility of number evolution by modeling the LF as an evolving Schechter function,

$$\Phi(L, z_s) dL = n_* (1 + z_s)^\beta \left(\frac{L}{L_*} \right)^\alpha e^{-L/L_*} \frac{dL}{L_*}. \quad (5)$$

We make both adjustments using the following technique. We first choose a value for the evolution parameter β . We postulate a set of Schechter function parameters (n_* , L_* , α) to specify the Λ CDM LF, $\Phi_{\Lambda\text{CDM}}$. We draw from this LF to generate a mock sample of sources in an Λ CDM universe. We then imagine “observing” these sources, interpreting them using an Λ CDM cosmology, and deriving the effective Λ CDM LF, $\Phi'_{\Lambda\text{CDM}}$. We compare $\Phi'_{\Lambda\text{CDM}}$ with the Λ CDM LF presented by Hogg et al. (1998) to see how well they match. We then repeat this process for many values of (n_* , L_* , α) and choose the values that provide the best match between $\Phi'_{\Lambda\text{CDM}}$ and the Hogg et al. data. This gives us the best-fit Λ CDM LF, for our particular choice of the evolution parameter β . Finally, we repeat the entire analysis for different values of β . The resulting LFs are summarized in Table 1.

With an LF of the form eq. (5), the luminosity integral in eq. (3) can be evaluated,

$$\int_{L_0/\mu}^{\infty} \Phi(L, z_s) dL = n_* (1 + z_s)^\beta \Gamma \left[1 + \alpha, \frac{L_0}{L_*\mu} \right], \quad (6)$$

where Γ is the incomplete gamma function. Recall that for a flux-limited survey, $L_0 = 4\pi(1 + z_s)^4 D_s^2 S_0$ depends on redshift.

3.3. Lens Population: SDSS LRG Sample

The initial sample analyzed by Bolton et al. (2004) included $\sim 51,000$ LRG spectra obtained by SDSS between 2000 March 5 and 2003 May 27. To obtain proper statistics, we must include appropriate distributions of z_l , σ , e , γ , and ϕ_γ for this sample (see eq. 4). The velocity dispersion function $dn/d\sigma$ of the full SDSS elliptical galaxy catalog has been measured by Sheth et al. (2003). Their analysis corrected for various selection effects in order to recover the intrinsic distribution $dn/d\sigma$. However, we wish to *include* the selection effects since our goal is to estimate how many rogue emission lines should have been found in the actual SDSS data.

To do this, and also to account for distributions of z_l and e , we randomly select 800 LRGs (see Eisenstein et al. 2001) observed between 2000 March 5 and 2003 May 27 and flagged as GALAXY-RED by the SDSS photometric pipeline (Lupton et al. 2001).⁷ The number of LRGs was chosen to be computationally tractable, and we have verified that it is a sufficiently large sample to yield accurate statistics (see §5.5). Choosing from the sample of observed LRGs automatically incorporates all of the same selection effects as the sample from which SLACS was drawn. As in Bolton et al. (2004), we restrict the LRG redshift range to $0.15 < z_l < 0.65$.⁸ We use r -band ellipticities from de Vaucouleurs fits in the SDSS photometric pipeline (Lupton et al. 2001). These ellipticities describe the light while what we really need is the mass, but there is evidence that the mass and light ellipticities follow similar distributions (Rusin & Tegmark 2001; Heyl et al. 1994; Naab & Burkert 2003).

We assign each galaxy a random shear amplitude drawn from a lognormal distribution centered on $\gamma = 0.05$ with dispersion 0.2 dex (see Holder & Schechter 2003), and a random shear angle $\phi_\gamma \in [0, 2\pi]$.

4. METHODS

Our formula for the total lensing probability explicitly includes two integrals over the source redshift z_s and the source position \vec{u} (see eq. 1). There is a third integral that enters implicitly: an integral over the image plane to compute the magnification of an extended source. The integral over source redshift is straightforward to compute numerically, but the 2-D integrals over the image and source planes require more care.

4.1. Semi-Analytic Image Plane Integration

To calculate the magnification μ for a given source and lens, we extend the analytic method developed in Dobler & Keeton (2005) to include finite source lensing by isothermal *ellipsoids* (SIEs) in an external shear field. The SIE density profile has been used quite successfully

⁷ For details related to SDSS, see York et al. (2000) for a technical summary, Gunn et al. (1998) for issues related to the camera, Fukugita et al. (1996), Hogg et al. (2001), and Smith et al. (2002) for a discussion of the photometric system and calibration, and Pier et al. (2003) for details related to astrometric calibration. The tiling procedure is described in Blanton et al. (2003).

⁸ The distributions of galaxies in redshift and velocity dispersion are shown in Figure 9.

to model not only quasar lenses but also the extended images seen in SLACS lenses (Koopmans et al. 2006). The lens equation is

$$\vec{u} = \begin{pmatrix} 1 - \gamma \cos 2\phi_\gamma & -\gamma \sin 2\phi_\gamma \\ -\gamma \sin 2\phi_\gamma & 1 + \gamma \cos 2\phi_\gamma \end{pmatrix} \vec{x} - \vec{\alpha}(\vec{x}), \quad (7)$$

where $\vec{x} = (r \cos \theta, r \sin \theta)$ are image plane coordinates. The two components of the deflection angle for an SIE lens are (Kormann et al. 1994; Keeton & Kochanek 1998)

$$\alpha_x = \frac{b'q}{\sqrt{1-q^2}} \tan^{-1} [Q(\theta) \cos \theta], \quad (8)$$

$$\alpha_y = \frac{b'q}{\sqrt{1-q^2}} \tanh^{-1} [Q(\theta) \sin \theta], \quad (9)$$

where $q = 1 - e$,

$$Q(\theta) = \left(\frac{1 - q^2}{q^2 \cos^2 \theta + \sin^2 \theta} \right)^{1/2}, \quad (10)$$

$$b' = \frac{b\pi}{2K(1+q^{-2})}, \quad (11)$$

and K is the complete elliptic integral of the first kind (see Huterer et al. 2005). The Einstein radius b of the galaxy is related to its velocity dispersion by

$$b = 4\pi \left(\frac{\sigma}{c} \right)^2 \frac{D_{ls}}{D_s}, \quad (12)$$

where D_s and D_{ls} are angular diameter distances from the observer to the source and from the lens to the source, respectively.

The idea behind our analytic method is to parameterize the source boundary by a circle: $(u, v) = (u_0 + R_{\text{src}} \cos \lambda, v_0 + R_{\text{src}} \sin \lambda)$ for $\lambda \in [0, 2\pi]$. Plugging this into the lens equation yields

$$\begin{aligned} u_0 + R_{\text{src}} \cos \lambda &= r \Gamma_- - \alpha_x, \\ v_0 + R_{\text{src}} \sin \lambda &= r \Gamma_+ - \alpha_y, \end{aligned} \quad (13)$$

with

$$\Gamma_\pm \equiv (1 \pm \gamma \cos 2\phi_\gamma) \cos \theta - \gamma \sin 2\phi_\gamma \sin \theta. \quad (14)$$

We square and add the two equations in eq. (13) to eliminate λ . Since α_x , α_y , and Γ_\pm are all independent of r , we obtain a simple quadratic equation for r that we can solve to find the following *analytic* expression for the image boundary as a function of θ :

$$r_\pm(\theta) = \frac{B \pm \sqrt{B^2 - AC}}{A} \quad (15)$$

where

$$\begin{aligned} A &= \Gamma_+^2 + \Gamma_-^2, \\ B &= \Gamma_- (\alpha_x + u_0) + \Gamma_+ (\alpha_y + v_0), \\ C &= (\alpha_x + u_0)^2 + (\alpha_y + v_0)^2 - R_{\text{src}}^2. \end{aligned} \quad (16)$$

The total magnification of an extended source is then

$$\mu_{\text{tot}} = \frac{\text{Total image area}}{\text{Total source area}} = \frac{1}{2\pi R_{\text{src}}^2} \int_{\mathcal{M}} (r_+^2 - r_-^2) d\theta \quad (17)$$

where \mathcal{M} is the region of θ over which $r_\pm(\theta)$ is real and positive. We can also impose the SDSS fiber cut very

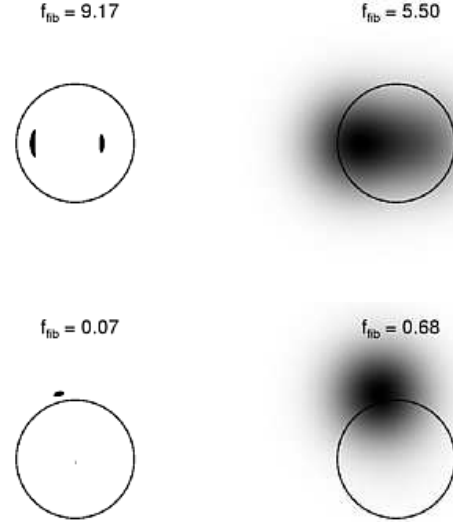


FIG. 3.— Sample image configurations for on-axis (top) and off-axis (bottom) lensing geometries both with (right) and without (left) seeing. Here $R_{\text{ein}} = 0.9$ arcsec and $R_{\text{src}} = 0.07$ arcsec, the source flux is normalized to unity, the circle represents the $r_{\text{fb}} = 1.5$ arcsec SDSS fiber, and the seeing is 2 arcsec (FWHM). For on-axis sources, the fiber flux is preferentially *decreased* due to seeing, while for off-axis sources the fiber flux is preferentially *increased*.

simply as follows. Let $r_{\text{fb}} = 1.5$ arcsec be the fiber radius. If we define the “fiber magnification” to be the total flux within the fiber divided by the total flux of the source, we can compute this as

$$\mu_{\text{fb}} = \frac{1}{2\pi R_{\text{src}}^2} \int_{\mathcal{M}} [\min(r_+, r_{\text{fb}})^2 - \min(r_-, r_{\text{fb}})^2] d\theta \quad (18)$$

We emphasize that in both cases the solution for the image boundary is completely analytic, which allows us to reduce the 2-D image plane integration to a 1-D integral along the image boundary.

It is useful to note explicitly where the various system parameters enter into the magnification calculation. The lens and source redshifts and the galaxy velocity dispersion all enter through the Einstein radius b . The shear parameters appear in Γ_\pm , while the ellipticity is buried in the deflection components α_x and α_y .

4.2. Seeing Effects

The above treatment of the image plane integration neglects the effects of atmospheric seeing. For the SLACS sample, the seeing is typically ~ 2 arcsec (FWHM), which is an appreciable fraction of the SDSS fiber diameter. Seeing can either *add* flux to the fiber from images outside, or *remove* flux from the fiber from images that are inside. Which of these effects dominates depends on the configuration of images, as shown in Figure 3.

We handle the effects of seeing in the following way. Let $I(\mathbf{x})$ be the surface brightness distribution of the lensed image (in the absence of seeing). Then the smeared surface brightness distribution is

$$I'(\mathbf{x}) = \int G(\mathbf{x} - \mathbf{x}') I(\mathbf{x}') d\mathbf{x}' \quad (19)$$

where G represents the PSF, which we take to be a Gaussian with FWHM 2 arcsec. Specifically, $G(\mathbf{x} - \mathbf{x}')$ is the flux at \mathbf{x} when the PSF is centered at \mathbf{x}' . The fiber flux is then

$$\begin{aligned} F_{\text{fib}} &= \int_{\text{fib}} I'(\mathbf{x}) d\mathbf{x} \\ &= \int_{\text{fib}} d\mathbf{x} \int d\mathbf{x}' G(\mathbf{x} - \mathbf{x}') I(\mathbf{x}') \\ &= \int d\mathbf{x}' I(\mathbf{x}') \left[\int_{\text{fib}} d\mathbf{x} G(\mathbf{x} - \mathbf{x}') \right]. \end{aligned} \quad (20)$$

The term in square brackets is the fiber flux of a Gaussian centered at \mathbf{x}' . Since the Gaussian PSF and the fiber are both circular, this term can only depend on the distance of the center of the Gaussian from the origin, $r = |\mathbf{x}'|$. Hence we write this factor as $G_{\text{fib}}(r)$, and then rewrite eq. (20) as

$$F_{\text{fib}} = \int_0^\infty dr r \int_0^{2\pi} d\theta I(r, \theta) G_{\text{fib}}(r). \quad (21)$$

If we take the source flux to be unity, the integral actually gives the fiber magnification μ_{fib} . In this case, the source surface brightness is $1/\pi R_{\text{src}}^2$, and since lensing conserves surface brightness we have $I(x) = 1/\pi R_{\text{src}}^2$ within the image boundaries, and 0 outside. Since the image boundaries are given by $r_\pm(\theta)$ from eq. (15), in the end we can write the fiber magnification in the presence of seeing as

$$\mu_{\text{fib}} = \frac{1}{\pi R_{\text{src}}^2} \int d\theta \int_{r_-(\theta)}^{r_+(\theta)} dr r G_{\text{fib}}(r), \quad (22)$$

which is a generalized version of eq. (18). The ‘‘fiber Gaussian’’ factor $G_{\text{fib}}(r)$ must be computed numerically, however this 1D integral only needs to be done once making this semi-analytic method for the image plane integration computationally orders of magnitudes faster than classical ray shooting methods for computing the magnification of an extended source.

4.3. Numerical Source Plane Integration

Since the magnification must be computed numerically, the source plane integral in eq. (1) must be computed numerically as well. The numerical integration scheme we use incorporates multiple grids with adaptive resolution to tile the source plane efficiently; details are given in the Appendix.

5. RESULTS

5.1. Three Probabilities

As discussed in §2, we use a magnification cut to determine whether a system is labeled a strong lens or not. Since the labeling is applied only after follow-up observations, we apply the cut to the total magnification (not the fiber magnification). We choose as our fiducial threshold $\mu_{\text{cut}} = 2$, because this corresponds to the magnification of a point source located on the boundary of the multiply-imaged region for an isothermal sphere lens. A finite source magnified by this amount should show clear signs of strong lensing. In other words, we define

$$P_L(\vec{G}; R_{\text{src}}) = P_G(\vec{G} \mid \mu_{\text{tot}}(R_{\text{src}}) > \mu_{\text{cut}}). \quad (23)$$

to be the probability that a galaxy has a rogue emission line due to a source that is lensed.

We should not just discard systems with magnifications below the cut. There is a range of positions (roughly speaking, behind the galaxy but outside the Einstein cone) where a source could send enough flux down the fiber to create a rogue line without being lensed. Such systems represent false positives in spectroscopic lens searches, and in order to understand the efficiency of a survey we need to assess the false positive rate. We define the complement of eq. (23) to be the probability that a galaxy has a rogue emission line due to a source that is *not* lensed:

$$P_N(\vec{G}; R_{\text{src}}) = P_G(\vec{G} \mid \mu_{\text{tot}}(R_{\text{src}}) < \mu_{\text{cut}}). \quad (24)$$

We can then let $P_R = P_L + P_N$ be the total probability that a galaxy has a rogue line, while $R_F = P_N/P_R$ is the false positive rate (defined to be the fraction of candidates for which follow-up observations do not show substantial evidence for lensing). Throughout our analysis we keep track of the total rogue line probability P_R , the lensing probability P_L , and the false positive rate R_F .

5.2. Back of the Envelope Estimate

Before giving our full results, we can make a simple estimate of the lensing probability. For this estimate we ignore finite source and fiber effects and just take all sources inside the Einstein cone to be lensed. For simplicity we take the luminosity threshold L_0 to be independent of source redshift, and we consider a non-evolving source luminosity function, so n_s is constant. If we let L_0 be the lowest luminosity threshold (i.e., computed from the flux limit S_0 at the minimum source redshift), we should overestimate the number of detectable sources. With these simplifications, the lensing probability is

$$\begin{aligned} P_L^{\text{est}} &\sim \int_{D_l^C}^{D_{s,\text{max}}^C} n_s \pi (D_s^C b)^2 dD_s^C \\ &\sim \int_{D_l^C}^{D_{s,\text{max}}^C} n_s 16\pi^3 \left(\frac{\sigma}{c}\right)^4 (D_s^C - D_l^C)^2 dD_s^C, \\ &\sim n_s \frac{16\pi^3}{3} \left(\frac{\sigma}{c}\right)^4 (D_{s,\text{max}}^C - D_l^C)^3. \\ &\sim n_s \frac{16\pi^3}{3} \left(\frac{\sigma}{c}\right)^4 \times \\ &\quad [(1 + z_{s,\text{max}})D_{s,\text{max}} - (1 + z_l)D_l]^3, \end{aligned} \quad (25)$$

where C indicates a comoving distance. We take $z_{s,\text{max}} = 0.9$. For fiducial LRG parameters $z_l = 0.2$ and $\sigma = 250$ km/s, our estimate yields $P_L^{\text{est}} \sim 3.1\%$. In other words, we expect the lensing probability to be at the percent level.

5.3. Dependence on Lens Parameters

We first seek to understand how the various probabilities depend on the lens galaxy properties. Figure 4 shows the rogue line probability, lensing probability, and false positive rate as a function of source size, for different values of the lens redshift z_l and velocity dispersion σ . The total probability P_R for detecting a rogue line in an LRG spectrum is at the level of 2–3% (consistent with

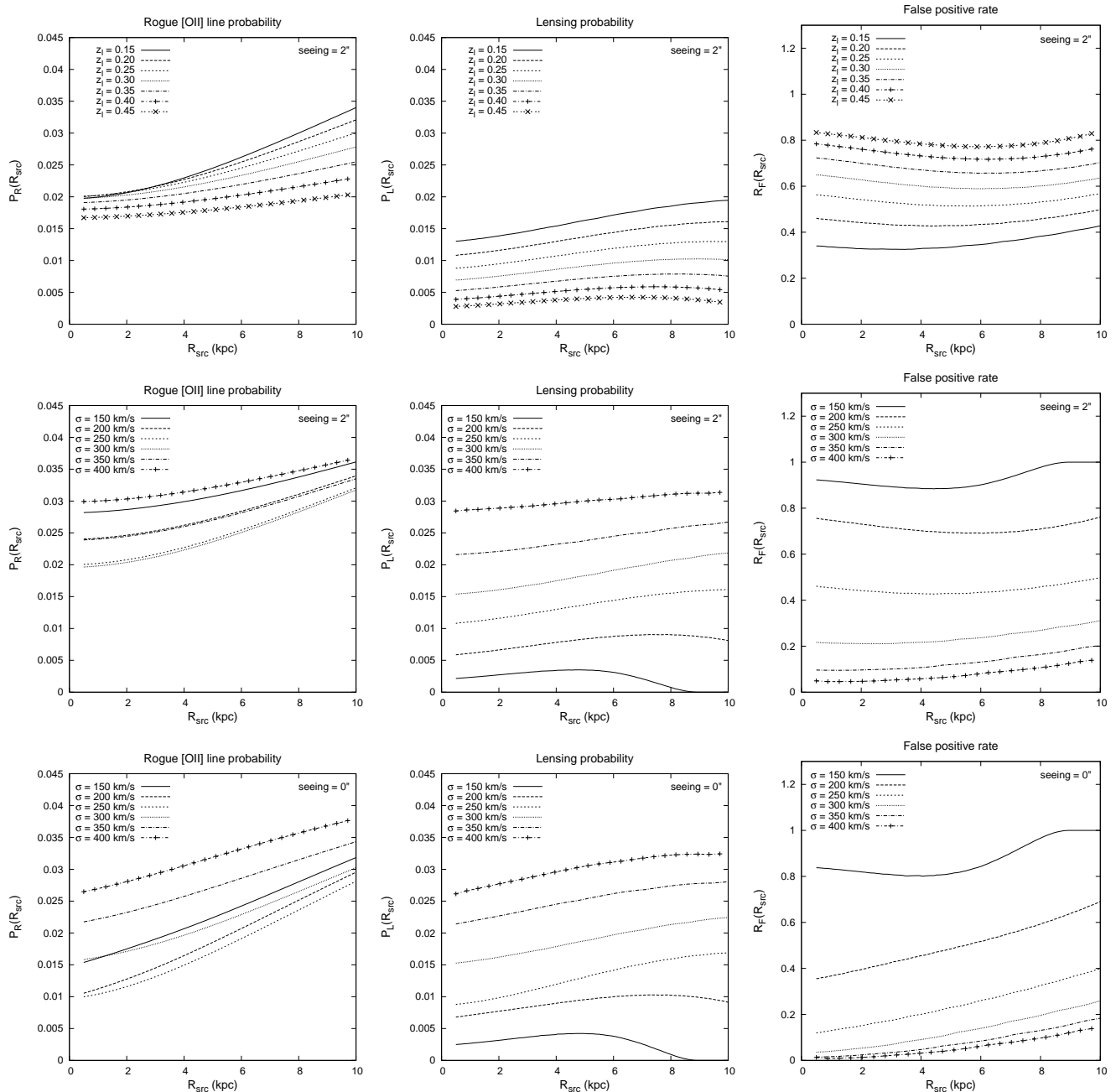


FIG. 4.— Total rogue line probability (P_R , left), lensing probability (P_L , middle), and false positive rate (R_F , right), as a function of the size of the source. We take as fiducial parameters $(z_l, \sigma, e, \gamma, \phi_\gamma) = (0.2, 250 \text{ km/s}, 0, 0, 0)$. In the top row we vary the lens redshift, in the middle row we vary the velocity dispersion, and in the bottom row we vary the velocity dispersion without including the effects of seeing. The spectroscopic fiber cut produces a non-monotonic dependence of P_R on σ . This behavior also depends on the seeing. The lensing probability P_L turns over at large R_{src} (most visible in the $\sigma = 150 \text{ km/s}$ curve) due to the magnification cut. The false positive rate also exhibits complex behavior with R_{src} and is very sensitive to both σ and z_l .

our estimate above), and depends moderately on lens redshift. Once a rogue line is detected, the probability that the line corresponds to a source that is significantly distorted decreases significantly with lens redshift: the false positive rate is only $R_F \sim 35\%$ at $z_l = 0.15$, compared with $R_F \sim 80\%$ at $z_l = 0.45$. The trend is not surprising because there is a finite upper limit on the source redshift, and the Einstein radius shrinks as the lens moves out in redshift ($b \propto D_{ls}$).

As expected, Figure 4 shows that the lensing probabil-

ity depends strongly on σ : P_L varies by almost a factor of 10 over the range $150 \text{ km/s} < \sigma < 400 \text{ km/s}$. For most values of σ , the lensing probability increases with source size over the range $0 < R_{\text{src}} < 10 \text{ kpc}$. However, for $\sigma = 150 \text{ km/s}$ the curve reaches a peak at $R_{\text{src}} \approx 5 \text{ kpc}$ and then turns over. We attribute this to finite source effects: at $\sigma = 150 \text{ km/s}$ the lens is simply not strong enough to significantly perturb a large source, ($R_{\text{ein}} = 0.48 \text{ arcsec}$ for $z_s = 0.9$). In fact, all of the P_L curves would turn over if we went to large enough source

size.

We also find the surprising result that the rogue line probability does not increase monotonically with σ . With 2 arcsec seeing, the ordering of the curves in increasing P_R is $\sigma = 300, 250, 350, 200, 150,$ and 400 km/s (for all source sizes). In other words, the total rogue line probability for $\sigma = 150$ km/s exceeds that for all other cases except $\sigma = 400$ km/s. We attribute this to the finite size of the spectroscopic fiber. When σ is small, the Einstein cone is small and most sources inside the fiber are not lensed (indeed, the false positive rate is high). As σ increases, lensing can push some of the light outside the fiber (see Figure 2), reducing the fiber flux and hence making the rogue line harder to detect. However, if the line is detected the chance that it corresponds to a lens is high. As σ increases still further, the Einstein cone begins to fill the fiber (the false positive rate becomes very low), and the rogue line probability increases with σ just like the lensing probability.

The total rogue line probability, and its non-monotonic dependence on σ , are sensitive to seeing. Eliminating seeing (bottom row of Figure 4) changes the ordering of the P_R curves with different values of σ ; in particular, it shifts the case with the lowest rogue line probability to lower σ . By contrast, seeing has less effect on the total lensing probability. These features can again be understood in terms of fiber effects. When σ is low, the Einstein radius is small and most of the “lens” configurations lie well within the spectroscopic fiber, so seeing has little effect on the fiber flux and hence on P_L . Seeing can pull flux into the fiber from sources that lie outside, but these are predominantly non-lens configurations. The net result is that seeing increases the total rogue line probability, mainly by adding false positives. When σ is high, by contrast, the fiber is mostly filled with “lens” configurations, so the false positive rate is low both with and without seeing.

Though not shown here, we have also studied the effects of varying ellipticity and shear parameters. We find no significant change in the lensing probability due to e and γ , in contrast to point source lensing statistics (Huterer et al. 2005). The difference is presumably related to the different statistical question (i.e., the probability that a galaxy is a lens rather than the probability that a source is lensed), and to effects like the fiber cut that are specific to spectroscopic surveys.

5.4. Dependence on Survey Parameters

It is important to understand the dependence of the probabilities on our choice of the definition of a lens (the magnification cut μ_{cut}), and on the survey noise floor S_0 . Figure 5 shows P_R , P_L , and R_F for $1.5 \leq \mu_{\text{cut}} \leq 3.0$. Since μ_{cut} simply indicates whether a source is classified as lensed or not, the rogue line probability does not change. However, the strong lensing probability P_L *does* depend on μ_{cut} . For $R_{\text{src}} = 0.5$ kpc, increasing μ_{cut} from 1.5 to 3.0 decreases the lensing probability by a factor of 2.4. At $R_{\text{src}} = 10$ kpc, the change is a factor of 4.1. The dependence on source size can be understood in terms of the magnification regions in the source plane. As μ_{cut} is increased, the total area of the source plane with $\mu > \mu_{\text{cut}}$ decreases more slowly for small sources than for larger sources.

If we double the noise floor S_0 , we find that the

rogue line probability is decreased by a factor of 0.65 for $R_{\text{src}} = 0.5$ kpc, and 0.63 for $R_{\text{src}} = 10$ kpc. This change is mainly caused by the number of sources brighter than the flux limit. Since $n_s \propto \Gamma[1 + \alpha, L_0/\mu L_*]$ and $L_0 \propto S_0$, doubling the noise floor changes the number of detectable sources by a factor of $\sim \Gamma[1 + \alpha, 2L_0/\mu L_*]/\Gamma[1 + \alpha, L_0/\mu L_*]$. This works out to be a factor of 0.6–0.8 for typical L_0 and μ values. This simple estimate agrees quite well with our full calculations despite ignoring complicated seeing effects, magnification effects, and the redshift dependence of L_0 .

5.5. Total Probabilities and Higher Order Statistics

We are now ready to compute overall probabilities by averaging over an appropriate sample of galaxies (see eq. 4). First we need to consider how many galaxies we need to include to obtain accurate statistics. Figure 6 shows the three probabilities as a function of the number of LRG realizations (for $R_{\text{src}} = 0.5$ kpc and $\beta = 0$, meaning no evolution in the source [O II] luminosity function). All three probabilities converge rather quickly, indicating that our fiducial sample size of 800 LRGs is sufficient.

Figure 7 shows the total probability for detecting rogue emission lines in LRG spectra, the probability of identifying lensing in follow-up observations, and the SLACS false-positive rate all as a function of source size averaged over our full sample of 800 galaxies.

At this point we also examine the effects of evolution of the source [O II] luminosity function. We consider four models, ranging from no evolution ($\beta = 0$) to a strong increase in the number of [O II] emitters in the past ($\beta = 3$). A value of $\beta \approx 2$ –3 for $z < 1$ is preferred by Glazebrook et al. (2003) based on SDSS derived star formation histories. LF evolution tends to decrease the rogue line and lensing probabilities. The explanation is that we fix the total number density of sources in the range $0.35 \leq z \leq 1.5$ from the observations by Hogg et al. (1998), so increasing β shifts a higher fraction of those sources to higher redshifts, and therefore *decreases* the number of sources below the SLACS upper limit $z_{s,\text{max}} = 0.9$.

For a source size of 0.5 kpc, we find the total probability for rogue line detection varies from 2.0% for source LF’s with no evolution ($\beta = 0$) to 0.9% for LF’s with strong evolution ($\beta = 3$). With $R_{\text{src}} = 10$ kpc, the probabilities are 3.0% ($\beta = 0$) and 1.3% ($\beta = 3$). The implication is that in the original Bolton et al. (2004) sample of 50,996 LRG spectra, ~ 460 –1,530 should contain rogue [O II] emission lines in their spectra above a threshold of 6×10^{-17} erg/s/cm². Of those, ~ 250 –640 should show significant strong lensing features when imaged with high spatial resolution. The remaining systems are false positive detections in which there is a background galaxy that is not significantly perturbed by lensing effects. The total false positive rate $R_F(R_{\text{src}})$ also varies significantly with with source size and β but has typical values $R_F \sim 50\%$ (see Figure 7). It is important to note that while the breakdown into lenses and false positives depends on our choice of the magnification cut ($\mu_{\text{cut}} = 2.0$), the total number of rogue lines is a robust prediction.

While our fiducial results have been computed for 2 arcsec seeing, it is instructive to consider how seeing affects our result. Figure 8 shows the three probabilities as a function of source size for various values of the seeing.

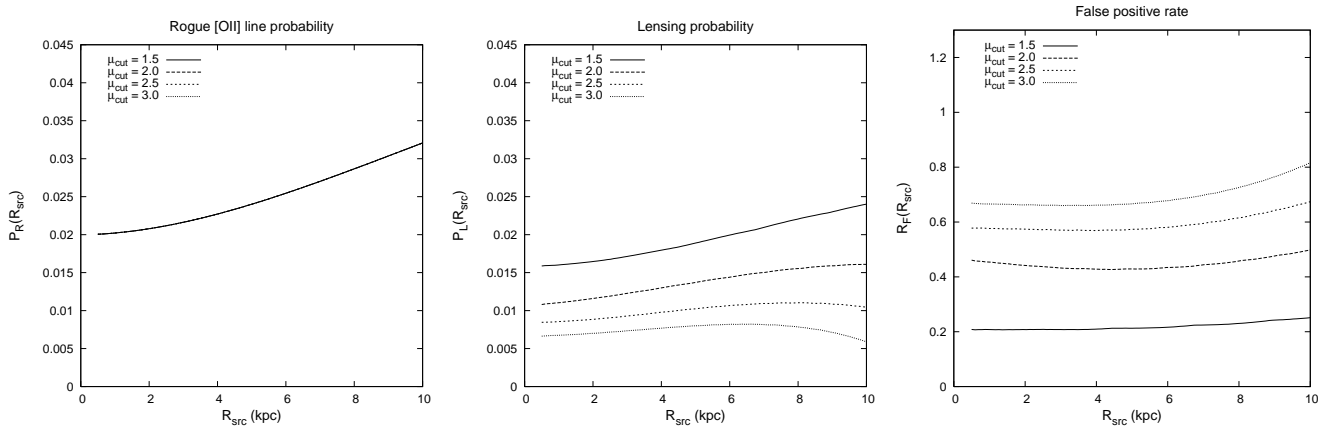


FIG. 5.— Same as Figure 4 except for varying μ_{cut} . The total number of rogue lines remains unchanged (of course), but the lensing probability P_L varies by a factor 2.4 at small source size and 4.1 at large source size. As expected, the false positive rate R_F is sensitively dependent on the definition of a lens, μ_{cut} .

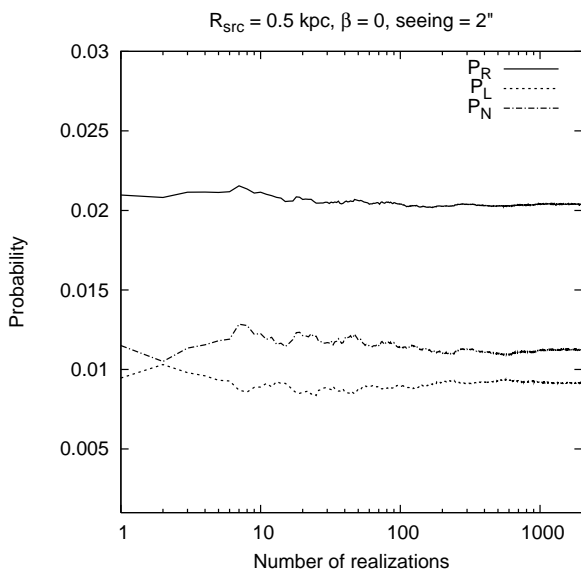


FIG. 6.— Total detection probabilities as a function of the number of LRG realizations. In this convergence test we fix the source size to be $R_{\text{src}} = 0.5$ kpc and we use a non-evolving source luminosity function ($\beta = 0$). The probabilities converge quickly, indicating that 800 realizations is more than adequate to yield accurate statistics.

The effect of seeing is to introduce a “tilt” to the lensing probability curve, giving a moderate boost at small source size and reduction at large source size. Seeing increases the total rogue line probability, especially at small source size. The implication is that seeing enhances the number of detected rogue lines that do not correspond to lens systems at all source sizes but most dramatically at small R_{src} . Indeed, the false positive rate increases monotonically with R_{src} when seeing is unimportant (the FWHM is small compared with the size of the spectroscopic fiber), while it flattens out and develops a minimum near $R_{\text{src}} \approx 5.5$ kpc when the seeing is important.

Although there is significant uncertainty due to source size and LF evolution effects, our lensing estimates are clearly higher than the ~ 150 rogue lines and ~ 60 lens

systems found in the initial SLACS sample. The most likely explanation for this discrepancy is that the SLACS selection criteria require two *additional* emission features ($H\beta$, [O III] 4959, or [O III] 5007) besides the primary [O II] 3727 line. The presence of these additional features was required to substantially reduce the number of false positives, but may have eliminated many real lens systems as well. Incorporating multiple emission line statistics into our calculations would require knowledge of the joint probability distribution between [O II] and secondary line luminosities and is beyond the scope of the present study. Furthermore, secondary lines tend to appear in the $\sim 7000\text{--}9000$ Å region of the spectrum where sky noise is more problematic; many spectra with secondary features buried in the noise may have been rejected as targets. In any event, we predict that there is a large number of g-g lenses waiting to be discovered in the SDSS spectroscopic data.

Finally, it is interesting to consider how the galaxies that produce g-g lenses may form a biased subset of all LRGs. Figure 9 shows the distributions of redshift and velocity dispersion for our parent population of galaxies, and for the same population with each galaxy weighted by its lensing probability (with $R_{\text{src}} = 0.5$ kpc, $\beta = 0$, seeing= $2''$). There is clearly a bias towards larger velocity dispersions, which is natural, but it is weaker than in traditional quasar lens statistics because of fiber cut effects. There is also a bias towards lower redshifts, because lower-redshift galaxies have larger Einstein cones (cf. Figure 4). We test the null hypothesis that the two populations represent the same probability distribution with the Kolmogorav-Smirnov test (Press et al. 1992). Comparing the distributions of the velocity dispersion (redshift) yields only a $2.5 \times 10^{-7}\%$ (0.05%) chance that the populations are drawn from the same distribution.

6. CONCLUSIONS

We have introduced a statistical method to estimate the expected number of strong galaxy-galaxy lens systems in a spectroscopic survey. In the process, we have also developed a semi-analytic technique for calculating the magnification of a finite source due to an isothermal ellipsoid galaxy in an external shear field. Conceptually, the most important result is that the size of the spec-

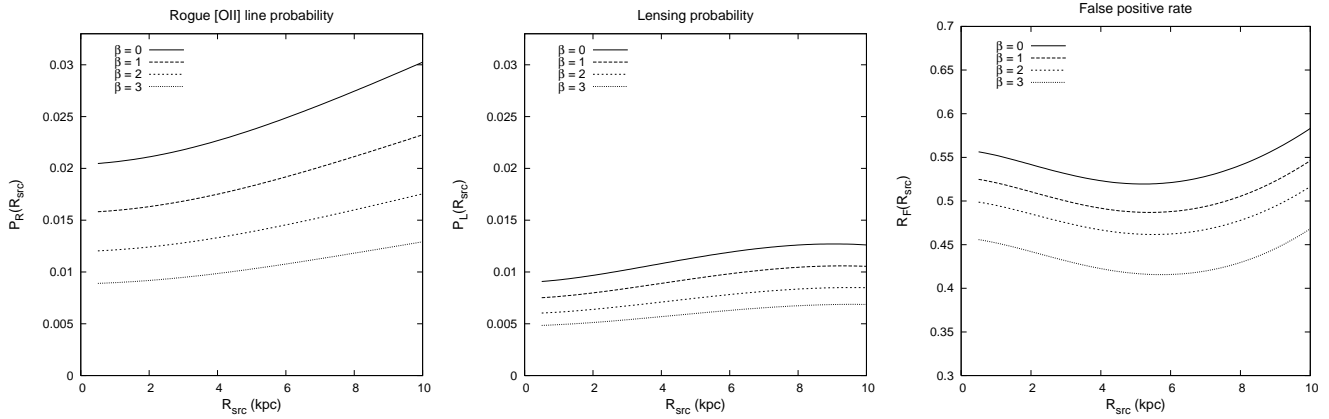


FIG. 7.— Total detection probabilities after averaging over 800 sets of LRG parameters, for four different models of LF evolution. Given these results, we expect that the initial SLACS sample of 50,996 LRGs should contain ~ 460 – $1,530$ galaxies with rogue emission lines in their spectra, and ~ 250 – 640 should reveal strong lensing features in follow-up observations.

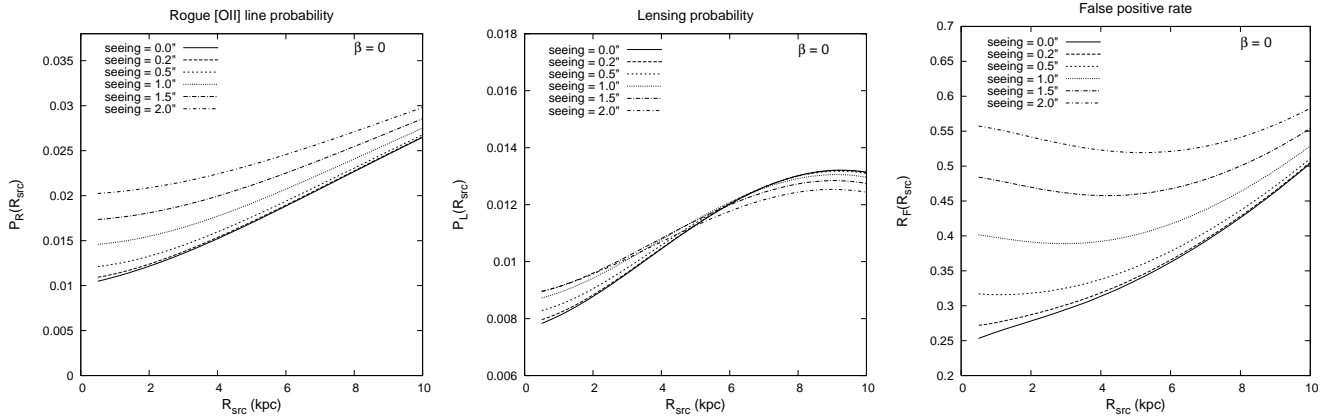


FIG. 8.— Total detection probabilities as a function of source size and the FWHM of the Gaussian seeing model ($\beta = 0$). Seeing effects boost the lensing probability at small R_{src} but suppress the lensing probability at large R_{src} . The total rogue line detection probability is boosted for all source sizes. The fraction of non-lenses is much more sensitive to seeing effects at small R_{src} leading to the minimum in the false positive rate in Figure 7.

troscopic fiber provides a significant selection effect. In our analysis of the SLACS survey, the fiber cut yields the unexpected result that the probability of detecting a rogue emission line is a non-monotonic function of the velocity dispersion σ . Since larger σ corresponds to a larger Einstein cone, one would naively expect the rogue line probability to increase with σ . However, large σ also corresponds to a large image separation, which can cause much of the source flux to fall outside the spectroscopic fiber. The situation is further complicated by the effects of atmospheric seeing which can add flux into the fiber from images outside or remove flux from the fiber from images inside. It will be crucial to compute the effects of the fiber cut and seeing, customized to the parameters of the spectrograph, for any future search for g-g lenses in large spectroscopic surveys.

The lensing probability has a fairly weak dependence on the size of the source, but a stronger dependence on the evolution of the source luminosity function. Lensing introduces biases such that lens galaxies will tend to have higher velocity dispersions and lower redshifts compared with the parent population of galaxies.

Incorporating parameters from the SLACS survey, we estimate that there should be ~ 460 – $1,380$ rogue emission lines in the sample of 50,996 LRG spectra. Of these, ~ 250 – 640 should show clear evidence of strong lensing in follow-up observations. The broad range of probabilities is due primarily to uncertainties in the physical size of [O II] emission regions and in the evolution of the [O II] luminosity function. Specifically, small sources and strong evolution yield lower probabilities while large sources and no evolution give higher probabilities. Our estimates are notably higher than the numbers actually observed in the SLACS survey so far. We attribute this to their requirement that multiple emission lines be detected, to the large amount of sky noise in the long wavelength region of the spectra, and to the potential extinction of the [O II] emission line by dust in the lens galaxies. Our calculations imply that there are many more galaxy-galaxy strong lenses waiting to be found in the SDSS spectroscopic data.

While our methods have been specifically applied to the SLACS survey, they should be applicable to all finite source lens searches in upcoming spectroscopic surveys.

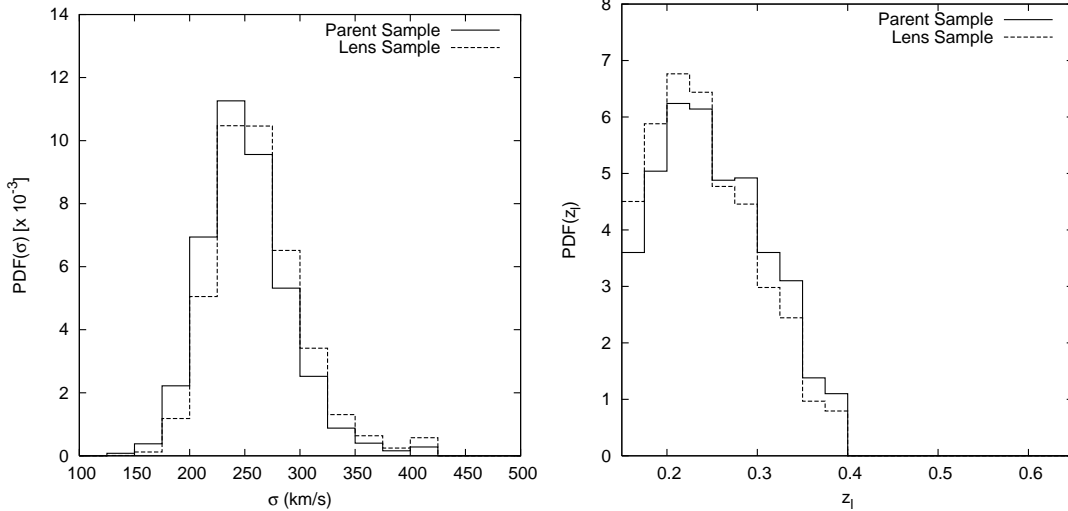


FIG. 9.— Histograms of velocity dispersion (left) and redshift (right), for the LRG parent sample (solid line) and the subsample that represent lenses (dashed line, $R_{\text{src}} = 0.5$ kpc, $\beta = 0$, seeing= $2''$). All histograms are normalized to unit area. The lens galaxies are biased towards higher velocity dispersion and lower redshift. A KS test comparing the distributions of the velocity dispersion (lens redshift) yields only a $2.5 \times 10^{-7}\%$ (0.05%) chance that the populations are drawn from the same distribution.

Future improvements to our method would involve incorporating non-uniform brightness distributions for the background source galaxies.

GD and CRK were supported in part by grant HST-

AR-10668 from the Space Telescope Science Institute, which is operated by the Association of Universities for Research in Astronomy, Inc., under NASA contract NAS5-26555.

REFERENCES

- Blanton M.R., Lin H., Lupton R.H., Maley F.M., Young N., Zehavi I., Loveday J., 2003, *AJ*, 125, 2276
 Bolton A. S., Burles S., Schlegel D. J., Eisenstein D. J., Brinkmann J., 2004, *AJ*, 127, 1860
 Bolton A. S., Burles S., Koopmans L. V. E., Treu T., Moustakas L., 2006, *ApJ*, 638, 703
 Bolton A. S., Burles S., Treu T., Koopmans L. V. E., Moustakas L., 2007, *ApJL* submitted, astro-ph/0701706
 Cabanac R. A. et al. 2007, *A&A*, 461, 813
 Dobler G., Keeton C. R., 2005, *MNRAS*, 365, 1243
 Dobler G., Keeton C. R., 2006, *ApJ*, 653, 1391
 Eisenstein D. J., Annis J., Gunn J. E. et al., 2001, *AJ*, 122, 2267
 Fukugita M., Ichikawa T., Gunn J. E., Doi M., Shimasaku K., and Schneider D. P. 1996, *AJ*, 111, 1748
 Gavazzi R. et al. 2007, submitted to *ApJ*, astro-ph/0701589
 Glazebrook K. et al., 2003, *ApJ*, 587, 55
 Gunn J. E., Carr M. A., Rockosi C. M., Sekiguchi M. et al. 1998, *AJ*, 116, 3040
 Heyl J. S., Hernquist L., Spergel D. N., 1994, *ApJ*, 427, 165
 Hogg D. W., Schlegel D. J., Finkbeiner D. P., and Gunn J. E. 2001, *AJ*, 122, 2129
 Hogg D. W., Cohen J. G., Blandford R., Pahre M. A., 1998, *ApJ*, 504, 622
 Holder G., Schechter P., 2003, *ApJ*, 589, 688
 Huterer D., Keeton C. R., Ma C. P., 2005, *ApJ*, 624, 34
 Keeton C. R., Kochanek C. S., 1997, *ApJ*, 487, 42
 Keeton C. R., Kochanek C. S., 1998, *ApJ*, 495, 157
 Kenicutt R. C., 1992, *ApJ*, 388, 310
 Kochanek C. S., 2002, *ApJ*, 578, 25
 Koopmans L. V. E., Treu T., Bolton A. S., Burles S., Moustakas L.A., 2006, astro-ph/0601628
 Kubo J. M. & Dell'Antonio I. P., 2007, arXiv:0712.3063
 Lupton R. H. et al., 2001, *ASPC*, 238, 269
 Marshall P., Blandford R., Sako M., 2005, *New AR*, 49, 387
 Moustakas L. et al. 2007, *ApJ*, 660L, 31
 Naab T., Burkert A., 2003, *ApJ*, 597, 893
 Oguri M., Kawano, Y., 2003, *MNRAS*, 338, L25
 Pier J.R., Munn J.A., Hindsley R.B., Hennessy G.S., Kent S.M., Lupton R.H., Ivezić Z. 2003, *AJ*, 125, 1559
 Press W., Schechter P., 1974, *ApJ*, 187, 425
 Press W.H., Teukolsky S.A., Vetterling W.T., & Flannery B.P., 1992, *Numerical Recipes in C*, 2nd edn., Cambridge, UK: Cambridge University Press
 Rusin D., Tegmark M., 2001, *ApJ*, 553, 709
 Kormann R., Schneider P., Bartelmann M., 1994, *A&A*, 284, 285
 Sheth R. K. et al., 2003, *ApJ*, 594, 225
 Smith J.A., Tucker D.L., Kent S.M. et al. 2002, *AJ*, 123, 2121
 Treu T., Koopmans L. V. E., Bolton A. S., Burles S., Moustakas L., 2006, *ApJ*, 604, in press
 Turner E. L., Ostriker J. P., Gott J. R. III, 1984, *ApJ*, 284, 1
 Warren S. J., et al. 1996, *MNRAS*, 278, 139
 Willis J.P., 2000, *Obs*, 120, 427
 Willis J. P., Hewett P. C., Warren S. J., Dye S., Maddox N., 2006, *MNRAS*, 369, 1521
 York D. G., Adelman J., Anderson J. E. et al. 2000, *AJ*, 120, 1579

APPENDIX

TWO-DIMENSIONAL INTEGRATION

Our source plane integration is carried out via a 2-D integrator that tiles the integration region efficiently by using a movable grid with adaptive resolution. As an example to illustrate our method, we first consider the magnification calculation for a uniform brightness finite source (with size R_{src} centered at the origin) which is lensed by an isothermal ellipsoidal mass distribution (SIE).

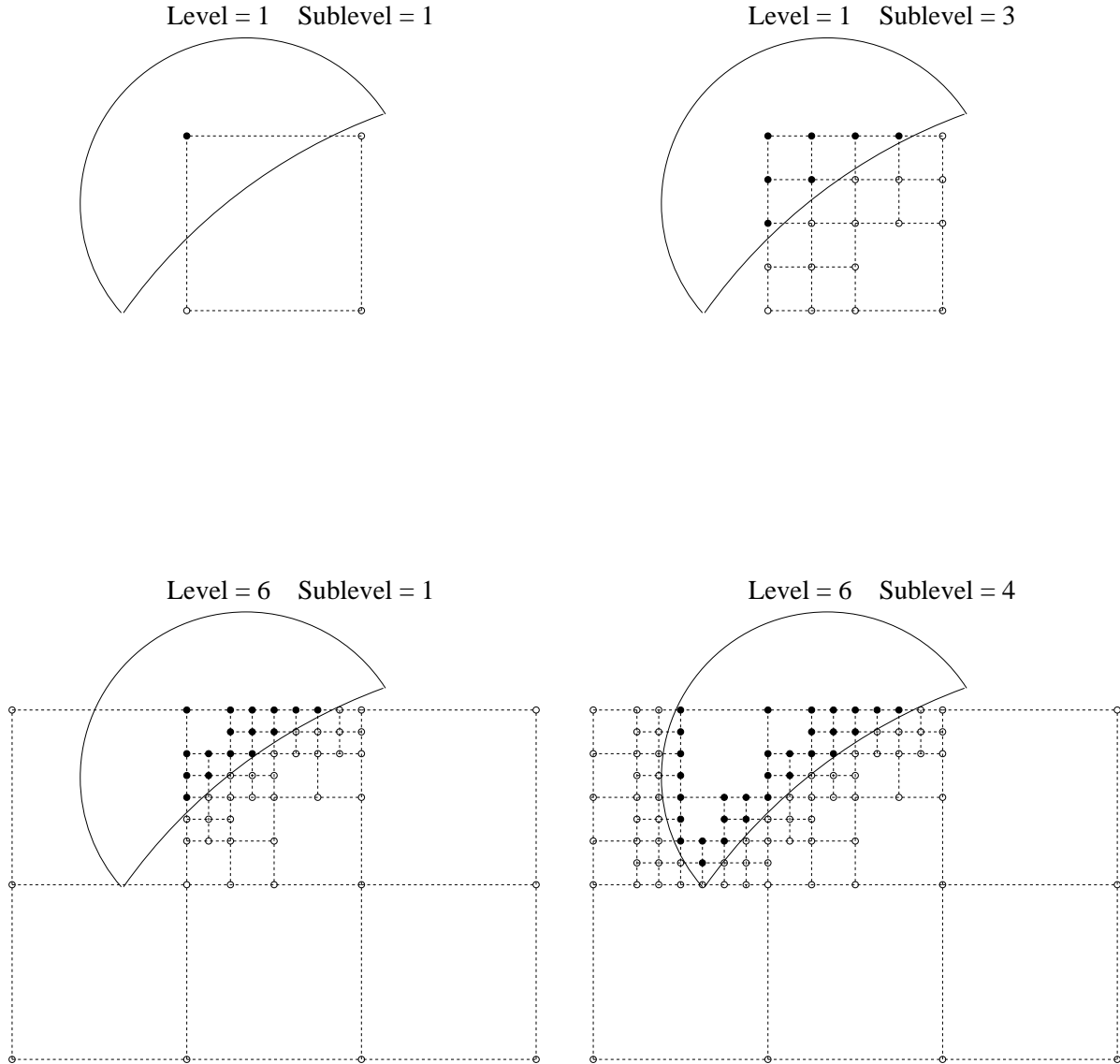


FIG. 10.— A schematic representation of the tiling algorithm. The algorithm uses a macrogrid with adaptive resolution that subdivides if the number of corners that are “in” is $\neq 0$ or 4. Once the maximum number of sublevels is reached, the macrogrid is shifted in a spiraling geometry about the origin.

Since the magnification is defined as,

$$\mu = \frac{\text{Area of the images}}{\text{Area of the source}}, \quad (\text{A1})$$

we must find the total area of the images by integrating over the 2-D image plane. We start with a single “macro”-grid whose lower right corner is centered on the origin and suppose that the edge of an image passes through this grid as shown in Figure 10. A grid point (x, y) is flagged as “in” if,

$$[x - \alpha_x(x, y)]^2 + [y - \alpha_y(x, y)]^2 \leq R_{\text{src}}^2 \quad (\text{A2})$$

and “out” if,

$$[x - \alpha_x(x, y)]^2 + [y - \alpha_y(x, y)]^2 > R_{\text{src}}^2 \quad (\text{A3})$$

Here $\vec{\alpha}(x, y)$ is the deflection angle due to the SIE at point (x, y) and relates the image plane grid points to the source plane coordinates (u, v) via the lens equation,

$$\begin{aligned} u &= x - \alpha_x(x, y) \\ v &= y - \alpha_y(x, y) \end{aligned} \quad (\text{A4})$$

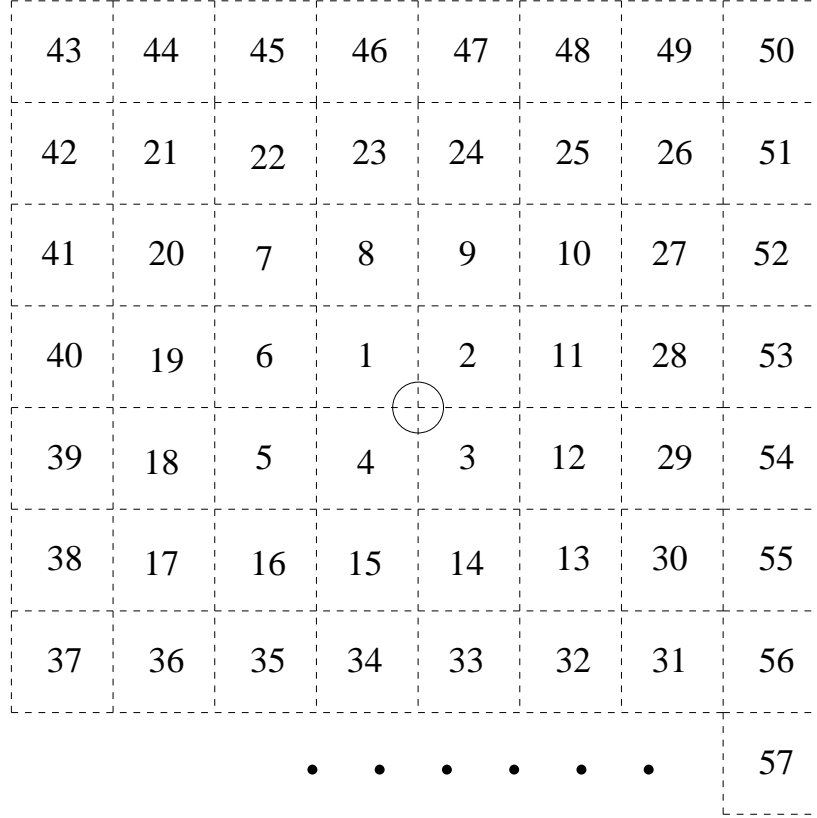


FIG. 11.— A schematic representation of the evaluation order for the “steps” for the spiraling algorithm. The origin is marked with an O and the spiraling terminates once N_{tol} revolutions yield no significant change in the integrated area.

We then recursively subdivide portions of this grid until all four corners of each subgrid are either “in” or “out” (or until the maximum number of subdivisions has been reached). For a given subgrid this implies that our criterion for further subdivision is:

$$\begin{aligned} N_{in} &= 1, 2, \text{ or } 3 && : \text{subdivide} \\ N_{in} &= 0 \text{ or } 4 && : \text{do not subdivide} \end{aligned} \quad (\text{A5})$$

where N_{in} is the number of corners that are flagged as being “in” the image.

Once this initial grid has been appropriately subdivided, we then move the macrogrid in a spiraling geometry and repeat the process (see Figure 11) keeping a running total of the image area upon each revolution of the spiral. This spiraling procedure self-terminates once the macrogrid has completed N_{tol} revolutions with little to no change in the total image area.

Our technique has the advantage of achieving high resolution with relatively few subdivisions per grid and, more importantly, does not require preset boundary conditions. That is, the self-termination criterion simply stops the spiraling procedure once the total image area is no longer changing. However, care must be taken to avoid missing “distant” images (images which appear far from the origin), and in practice we do set a minimum number of revolutions for the spiral.

In the previous example, we assumed our function evaluations at the grid points took only two values: 1 or 0 (i.e., “in” or “out” of the image). The next step is to allow each grid point to assume a continuous value $f(x, y)$. With this generalization, we must modify our subdivision criterion which we now take to be,

$$\begin{aligned} |F_{avg} - F_c| &\geq \epsilon |F_{avg}| && : \text{subdivide} \\ |F_{avg} - F_c| &< \epsilon |F_{avg}| && : \text{do not subdivide,} \end{aligned} \quad (\text{A6})$$

where

$$F_{avg} = \frac{1}{4}[f(x_1, y_1) + f(x_2, y_1) + f(x_1, y_2) + f(x_2, y_2)] \quad (\text{A7})$$

is the average of the function values at the four grid corners and,

$$F_c = f\left(\frac{x_1 + x_2}{2}, \frac{y_1 + y_2}{2}\right) \quad (\text{A8})$$

is the function value at the center of the grid. The tolerance value ϵ must be set by hand and is roughly a measure of how much $f(x, y)$ varies over the region $[x_1 : x_2][y_1 : y_2]$. That is, our grid only increases resolution in regions where the function varies rapidly with either x or y . Since the spiral termination criterion is still such that the total integral

does not significantly change after N_{tol} revolutions, this 2-D integration scheme is ideally suited to integrate functions for which $f(x, y) \rightarrow 0$ as $x, y \rightarrow \infty$.